COBEM 2023 27TH INTERNATIONAL CONGRESS OF MECHANICAL ENGENEERING

ABCM Brazilian Society of Mechanical Sciences and Engineering
27th ABCM International Congress of Mechanical Engineering
December 04-08, 2023, Florianópolis-SC, Brazil

COB-2023-2333
A PRELIMINARY NUMERICAL STUDY OF A THERMAL MANAGEMENT SYSTEM FOR ELECTRIC VEHICLE BATTERIES EMPLOYING MICROCHANNELS WITH TRIPLY PERIODIC MINIMAL SURFACES

Felipe Pereira Neto Selmo
Guilherme Henrique Fiorot
Universidade Federal do Rio Grande do Sul, Porto Alegre, Brazil
felipe.selmo@outlook.com
guilherme.fiorot@ufrgs.br

Abstract. *The increasing use of electric and hybrid cars stimulates the need for improvement of autonomy and safety of the energy storage systems of these vehicles. In this context, Battery Thermal Management Systems (BTMS) assume a fundamental role: they seek to guarantee an adequate thermal condition in the battery cells. On the other hand, the growth of additive manufacturing techniques expands the possibility of investigating different topologies that seek to improve heat transfer in these systems. In this sense, Triply Periodic Minimal Surfaces (TPMS) can be an option to achieve this once they offer high surface-area-to-volume ratios and high heat transfer area. Using the software OpenFOAM®, the present work aimed to numerically study the effects of the use of Schwarz Type-D TPMS-based structures in the tubes of a BTMS considering a steady-state process of indirect liquid cooling of cylindrical lithium-ion battery cells. Results showed that the employment of a TPMS geometry offers, in comparison to a baseline system, a reduction in the maximum temperature of the cell set by more than 2K and a increase of the Nusselt number by a factor of* 3.11*, but increases the friction factor in the cooling tubes. This scenario indicates that the application of the studied TPMS system prioritizes a better thermal operation of the battery cells over a high friction factor.*

Keywords: *Electric vehicles, BTMS, TPMS, OpenFOAM*

1. INTRODUCTION

Electric vehicles can present a series of benefits when compared to vehicles with Internal Combustion Engines, such as greater energy efficiency of the vehicle and the ability to reduce Greenhouse Gas (GHG) emissions when associated with power systems with low GHG (International Energy Agency, 2020). Furthermore, electric vehicles gain relevance in the current development of energy policies in different countries, motivating policies such as the Fit-for-55 package of the European Union, which encourages the transition to electric and hybrid vehicles (International Energy Agency, 2022).

The results of these policies drove the growth of the electric vehicles industry in regions such as China, Europe and the US. An example of that is the increase by a factor of 2.42 of the combined sales of plug-in and battery electric cars on Europe from 2019 to 2020 (International Energy Agency, 2022). Nevertheless, the improvement and development of electric vehicles, particularly related to batteries, represents a constant challenge for this industry according to Deng *et al.* (2018).

In this sense, a Battery Thermal Management System (BTMS) of an electric vehicle is essential to improve both safety and life cycle of the battery system, specially lithium-ion batteries, which are widely used in the automotive industry and are very sensitive to temperature changes (Kim *et al.*, 2019). According to Ianniciello *et al.* (2018), maintaining the battery operation within a small temperature range through time avoids the reducing of the capacity and autonomy of the cells.

Several types of BTMS are modeled to evaluate the cooling process during battery discharge. In this context, systems with liquid and air cooling were compared in the work by Han *et al.* (2019). The authors found very different typical values for the ratio between the rate of heat transferred from the battery cells to the fluid and the difference between their average temperature and the inlet temperature of the fluid: 500 W/K for the first type and 70 W/K for the second type, indicating a potential better cooling capacity of systems employing liquids.

For battery packs composed by cylindrical cells, different configurations are studied considering variations of flow pattern and geometric parameters of the BTMS. Applied to this type of battery, systems that have microchannels and extended surfaces achieve good results in the thermal control of the battery. In the work by Rao *et al.* (2017), a liquid cooling system employing water was studied. The parametric analysis showed that larger diameters of the microchannels result in greater temperature uniformity in the cells and high inlet velocities drastically reduce the maximum temperature

of the cells.

Furthermore, systems that use coils coupled to metal blocks can meet thermal operation requirements, but with a limitation on the system's operating power according to the volumetric flow. In the work of Wang *et al.* (2020), it was observed a fast drop in the maximum temperature of the cells and an adequate uniformity of temperatures in parallel flow arrangement, keeping the maximum temperature difference lower than 4.17°C.

In order to increase the contact area, Tete *et al.* (2022) proposed a geometry that encapsulates the cylindrical cells, isolating them from the fluid (water), with the tubes presenting a parallel flow scheme. The BTMS was simulated for different battery discharges: for a discharge interval of 0.5 to 5C, the average temperature of the batteries was maintained below 30°C. Furthermore, temperatures were higher for inner cells of the array although the maximum temperature difference is less than 3°C.

With a similar objective, Fan *et al.* (2022) developed a modular system of cooling cylindrical cells, employing structures based on Triply Periodic Minimal Surfaces (TPMS) to compose bundles of tubes contained inside a metal block (composing the thermal exchange interface between fluid and battery). These structures are characterized by a large surface-area-to-volume ratio, which is beneficial for compact heat transfer systems since the internal components of the tube increase the heat transfer area from the tube wall to the coolant. The authors constructed different tubes using TPMS-based on the Schwarz Type-P surface and compared this topology with straight tubes. At the end of a 2C discharge, despite the pressure drop increasing significantly, the maximum temperature difference for the first system is below 1.5°C while for the second one is above 2.5°C.

In order to investigate another type of triply periodic minimal surface, Attarzadeh *et al.* (2021), studied the effect of different structures based on a Schwarz Type-D TPMS inside a pipe with partially heated wall and steady-state flow. The best results ensured a Nusselt number above 40 for the entire simulated Reynolds (Re) range (25 to 125) which represents more than double when compared to the system without the structure. However, the pressure drop in the system with TPMS presented a behavior proportional to the square of the Reynolds number, which can be a problem when operating with high Re.

Thus, this work aims to numerically study the effect of structures based on Schwarz Type-D TPMS inside tubes of a liquid cooling BTMS for a electric car battery composed by by lithium-ion cylindrical cells. For that, steady-state simulations of the cooling system with and without the TPMS-based structure were done using the *chtMultiRegionFoam* solver from the OpenFOAM® software in order to simulate the conjugated heat transfer and flow inside the tubes.

2. TRIPLY PERIODIC MINIMAL SURFACES

Triply Periodic Minimal Surfaces are surfaces that are periodic in the three spatial dimensions, minimize the surface area in a delimited spatial region and present null local mean curvature (Assis, 2021). These surfaces can be implicitly described by a $\gamma(x, y, z)$ surface equation, such as the Schwarz TPMS Type-D equation – defined by Eq. (1) (Rajagopalan and Robb, 2006). The angular frequency ω of the TPMS is defined by Eq. (2) where l is the periodic length and c is the surface level parameter delimited by the region within $-l/2 \leq x \leq l/2$, $-l/2 \leq y \leq l/2$ and $-l/2 \leq z \leq l/2$ (Fan *et al.*, 2022).

$$\begin{aligned}\gamma(x,y,z) = {} & sen(\omega x)sen(\omega y)sen(\omega z) + sen(\omega x)cos(\omega y)cos(\omega z) \\ & + cos(\omega x)sen(\omega y)cos(\omega z) + cos(\omega x)cos(\omega y)sen(\omega z) = c\end{aligned} \tag{1}$$

$$\omega = 2\pi/l \tag{2}$$

The construction of TPMS-based structures is helped by the recent growth of additive manufacturing techniques (Attarzadeh *et al.*, 2021). In this context, one way to build them is to define two surfaces - $\gamma_1(x, y, z) \leq -c$ and $\gamma_2(x, y, z) \leq c$ - and define a volume within these surfaces (Al-Ketan *et al.*, 2021), thus assigning a thickness to the solid which is controlled by the level c. An example of a Schwarz Type-D structure constructed by the previous method is illustrated in Fig. 1.

The application of these structures in heat exchangers and similar systems is specially motivated by the fact that a TPMS divides the region into two separate sub-regions (Peng *et al.*, 2019). This can intensify the heat transfer process since the flow is established in a parallel and separated way considering these two sub-regions, thus there is a high interface area between fluid and heated/cooled walls. Furthermore, the property of high surface-area-to-volume ratio is an important topological attribute in these applications (Peng *et al.*, 2019) once the the weight and volume of the tube structures are relevant design issues.

3. GEOMETRY

The baseline geometry is based on submodules of six battery cells in series and eight in parallel (6S8P configuration), used for instance in the work of He *et al.* (2022). The cells are inside an aluminum metal block. Between sets of cells rows,

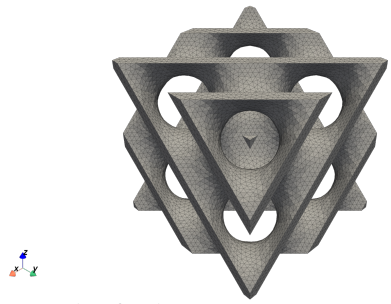

Figure 1: Example of Schwarz Type-D TPMS-based unit structure.

there are three cooling tubes, T1, T2 and T3, which have square inlets and outlets. In order to reduce the computational cost of the numerical simulations, two symmetry plans are introduced, which have their normal vectors parallel to the y axis. This is a simplification similar to the one in the work of Fan *et al.* (2022).

Thus, the geometry is composed of different regions: sixteen battery cells, a metal block and three cooling tubes. In this work, two configurations will be explored: baseline system, with straight cooling tubes; and a TPMS system, with a TPMS-based structure placed inside the cooling tubes. Schemes of the xy and yz planes can be found at Fig. 2(a), which provide the numbering of the battery cells. The geometric parameters are shown in Tab. 1.

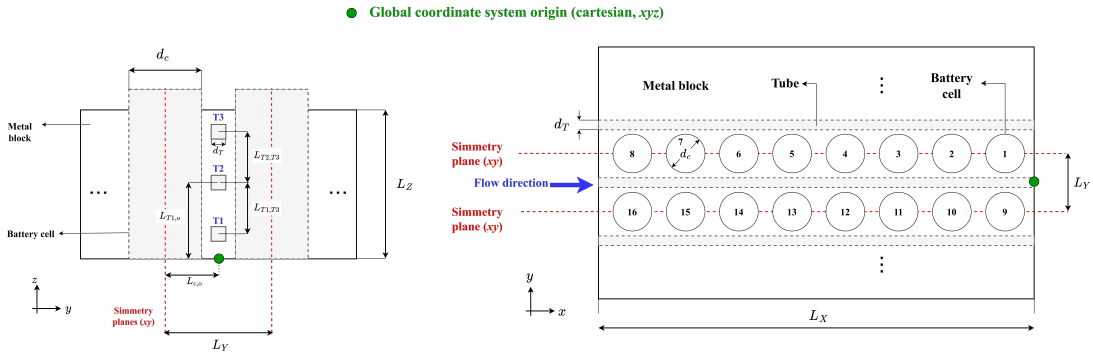

(a) Batteries positioning and schematics of the xy and yz planes.

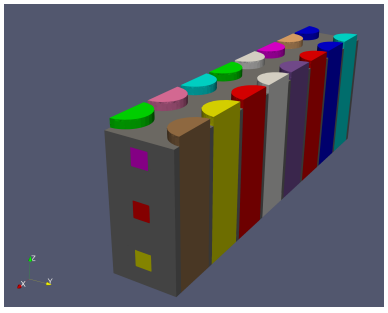

(b) Three-dimensional view.

Figure 2: Schematics of the baseline system.

A three-dimensional view of the baseline geometry is provided in Fig. 2(b). The TPMS system is made of tubes whose geometries are arrays of a TPMS' fluid domain unit structure. This structure is constructed from a boolean operation between a rectangular fluid domain unit from baseline tube and a unit wall structure based on Schwarz Type-D TPMS (see Section 2 for more details). The periodic length and the surface level parameter of the TPMS-based structure are respectively 8×10^{-3} m and 0.3. This construction process is illustrated at Fig. 3.

4. MATHEMATICAL AND NUMERICAL MODELING

Fluid flow and convection in the cooling tubes and conduction in the metal block and battery cells regions can be modeled by the generic conservation equation given by Eq. (3) (Versteeg and Malalasekera, 2007). The generic conserved intensive property ϕ assumes: 1 for mass conservation; u, v and w for momentum conservation in, respectively, x, y and z directions; and, for energy conservation, specific enthalpy h for convection modeling and specific internal energy e for

Table 1: Dimensions of geometry.

Dimension	Value
L_x, m	192×10^{-3}
L_y, m	32×10^{-3}
L_z, m	66×10^{-3}
d_T, m	8×10^{-3}
$L_{c,o}$, m	16×10^{-3}
$L_{T1,o}$, m	35×10^{-3}
$L_{T1,T2}$, m	23×10^{-3}
$L_{T2,T3}$, m	23×10^{-3}

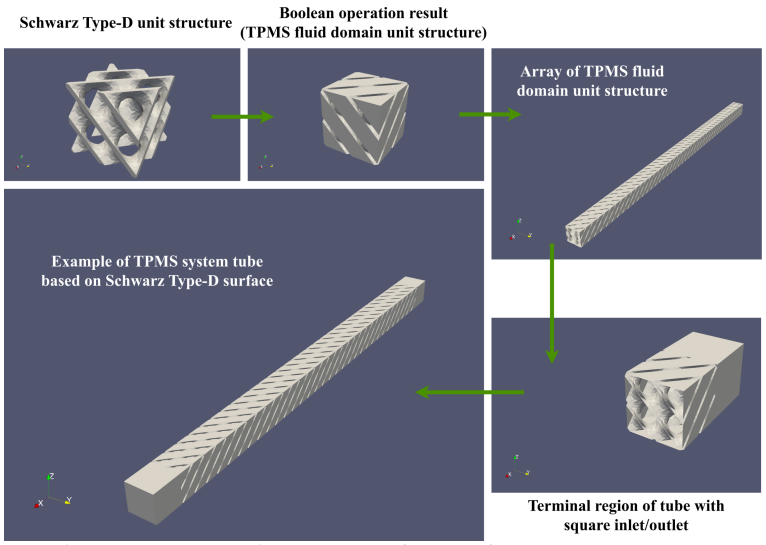

Figure 3: Construction process of a tube for the TPMS system.

conduction modeling.

$$\frac{\partial(\rho\phi)}{\partial t} + \vec{\nabla} \cdot (\rho\phi\vec{V}) = \vec{\nabla} \cdot (\Gamma\vec{\nabla}\phi) + S_\phi \tag{3}$$

The diffusion coefficient Γ is the thermal conductivity k when ϕ assumes e (solid material) or h (fluid material). If ϕ assumes u, v or w, then Γ is the dynamic viscosity μ of the fluid. Considering all physical phenomena in steady-state and thermal viscous dissipation insignificant, then the source terms are detailed in Tab. 2, being P the pressure field and $\dot{q}$ the volumetric heat generation which is differentiated for h and e by their respective subscripts.

Table 2: Source terms according to different ϕ.

Conservation	ϕ	S_ϕ
Mass	1	0
Energy	e	$\dot{q}_e$
	h	$\dot{q}_h$
Momentum	u	$-\frac{\partial P}{\partial x}$
	v	$-\frac{\partial P}{\partial y}$
	w	$-\frac{\partial P}{\partial z}$

Moreover, the following hypothesis are considered: the flow inside the tubes is considered to be incompressible and laminar; the transport and thermophysical properties are taken as constant and uniform (see Tab. 3); the volumetric heat

generation in the metal block and fluid regions is considered zero; and the thermal contact resistance at regions interfaces are negligible.

Table 3: Thermophysical and transport properties.

Domain Region	Material	Property	Value
Metal block and tubes walls	Aluminum	ρ, kg/m³	2699.2
		C_p, J/(kg·K)	897
		k, W/(m·K)	237
Fluid	Saturated water (25°C)	ρ, kg/m³	996.9
		C_p, J/(kg·K)	4182.6
		k, W/(m·K)	0.606
		μ, kg/(m·s)	890 $\times 10^{-6}$

Regarding the modeling of heat generation inside the battery cells, it is considered the time-averaged heat generation from the experimental data of a 21700 NCM811 battery cell extracted from the work of Wang *et al.* (2021). The measurements are related to a full 2C discharge and the time-averaged volumetric heat generation calculated is 1675.48 W/m³.

The boundary conditions are displayed by domain region according to Tab. 4. In order to simulate the cooling process exclusively due to the cooling tubes, the external surfaces of the domain are considered adiabatic. With respect to the interface walls (the cell-metal block interface and the fluid-cooling tube interface), they are considered as mapped walls (coupled temperature). Lastly, because the tubes' inlet velocity u is prescribed for both systems and they have the same square inlet section, the mass flow in the tubes is the same for both systems ($0.536 \times 10^{-}3$ kg/s).

Table 4: Boundary Conditions.

Domain Region	Surface	Boundary condition
Metal block	External surfaces	Adiabatic
Battery cells	Surfaces with no contact with metal block	Adiabatic
Tubes (T1, T2, T3)	Inlet	$u = 0.0084$ $v = 0$ $w = 0$, m/s | $T = 298$, K
	Outlet	$P = 0$, Pa
	Walls	No-slip

The hydraulic diameter (D) of the tubes in the baseline system is calculated by Eq. (4) (Incropera, 2007), where $\not{V}_t$ is the tube volume occupied by fluid the and A_f is the interface area between tube wall and fluid. For the TPMS system, D is calculated by Eq. (4) as well (Tang *et al.*, 2023). The surface-area-to-volume ratio, as mentioned in Section 2, is given by $A_f/\not{V}$.

The hydraulic diameter and geometric parameters of both systems are compared in Tab 5. It is shown the main geometric benefit of structures based on triply periodic minimal surfaces: the increase of A_f, representing a growth of more than 150 %. In addition, the surface-area-to-volume ratio of the tube increases by more than 225 %, which is a desirable aspect considering possible volume and mass concerns of the BTMS in an automotive context and the goal of the cooling system to be more compact.

$$D = \frac{4\not{V}_t}{A_f} \tag{4}$$

Table 5: Geometrical parameters comparison.

Parameter	Baseline system	TPMS system
A_f, m²	6.144×10^{-3}	15.714×10^{-3}
$A_f/\not{V}_t$, 1/m	500	1628
D, m	8.000×10^{-3}	2.457×10^{-3}

The version 10 of OpenFOAM® software was used to create the mesh and simulate the fluid flow inside tubes and the conjugate heat transfer between the different regions present in the overall simulation domain (battery cells, metal block, fluid region inside tubes). For that reason, *snappyHexMesh* mesher and *chtMultiRegion* solver were employed. To access and extract scalar fields data for postprocessing activities, the version 5.1.0 of Paraview® software was used alongside Python scripts for data treatment, calculations and plots.

Furthermore, because of the periodic characteristics of TPMS-based structures used in cooling tubes, flow and heat transfer properties can be analyzed using the Discrete Time Fourier Series (DTFS). This Fourier analysis originally uses a frequency domain from a time-based series, but the current analysis evaluates spatial-based quantities, there is, physical properties along the cooling tube (x axis). Therefore, it is adopted the wavenumber κ (physical unit 1/m) as the transformed domain of these spatial-based variables, which is an analogy to the frequency.

Lastly, heat transfer and flow average parameters are calculated locally (evaluated at sections with fixed x axis values) and globally (whole tube domain). Considering the definition of local convection coefficient from Incropera (2007), then the local average Nusselt number ($\overline{Nu}_x$) is defined by Eq. (5), being T_w the wall temperature (K), T_b the bulk temperature (K), q" the heat flux (W/(m²K)) at the wall and k_f the fluid's thermal conductivity. For all the tube domain, the global average Nusselt number ($\overline{Nu}$) is calculated using Eq. (6).

Similarly, the global average friction factor ($\overline{f}$) is given by Eq. (7), being u_m the mean u velocity (m/s). The quantities T_b and u_m are evaluated at cross sections of the tube with surface area A_c which has normal vector parallel to x. Finally, the local average of the magnitude of the velocity field ($\overline{||\vec{V}||}_x$) is calculated using Eq. (8).

$$\overline{Nu}_x = \frac{D}{k_f}\left[\frac{1}{A_c}\int_{A_c}\left(\frac{q"}{T_w - T_b}\right)dA\right] \tag{5}$$

$$\overline{Nu} = \frac{D}{k_f}\left[\frac{1}{\forall_t}\int_{\forall_t}\left(\frac{q"}{T_w - T_b}\right)d\forall\right] \tag{6}$$

$$\overline{f} = \frac{1}{\forall_t}\int_{\forall_t}\left(-\frac{\partial P}{\partial x}\frac{D}{\rho u_m^2/2}\right)d\forall \tag{7}$$

$$\overline{||\vec{V}||}_x = \frac{1}{A_c}\int_{A_c}||\vec{V}||dA \tag{8}$$

5. MESH QUALITY STUDY

For the mesh quality study, the methodology defined in the work by Celik *et al.* (2008) was used. Field values were extracted from five probes within the multiregion domain for each one of the systems simulated (baseline and TPMS) as it follows: temperature in cell 1; temperature in cell 16; and temperature, u and P in tube T1. Three meshes with different number of cells were analyzed separately for each system. Regarding the baseline system, the following meshes were considered: mesh A (1,933,480 cells), mesh B (559,192 cells) and mesh C (199,808 cells). For the TPMS system, the following meshes were considered: mesh A (4,687,662 cells), mesh B (2,382,486 cells) and mesh C (467,619 cells).

For both the baseline and the TPMS systems, the Grid Convergence Indexes (GCI) were below 1.0 % in relation to the temperature probes for the two comparisons (meshes B and C, and meshes A and B), being considered a satisfactory result. However, the GCI values for pressure and velocity probes, for both systems, were considered high in the analysis between meshes B and C: 8.19 % for u and 7.48 % for P.

Therefore, meshes A (more refined) were chosen for the post-processing analysis for both systems, because they presented lower values of uncertainty associated with the discretization of the domain. For these meshes, the GCI associated with pressure was below 5 %, while the GCI associated with velocity was 6.10 %.

6. RESULTS AND DISCUSSION

A comparison of general parameters of the baseline and TPMS-based systems is displayed in the Tab. 6. Given that the same inlet mass flow was considered for both systems, it was observed that the Reynolds number is lower in TPMS-based tubes since there is a reduction of 69.29 % of the hydraulic diameter.

The increase of interface area between the metal block and fluid due to the TPMS-based structures ultimately intensifies heat transfer. This is examplified comparing the two local average Nusselt numbers: the system with tubes with TPMS structures presents, on average, values 3.11 higher than the baseline system.

Although there is an increase in heat transfer, the global average friction factor in the tubes of the TPMS system is 21.37 times larger than the one found in the baseline system. This behavior is explained from the characterization that the flow has in tubes filled by structures based on TPMS: the augmentation of fluid-wall interface leads to more friction and there is more stagnation regions due to the presence of internal walls opposing to the flow.

Regarding the distribution of temperatures in the battery cells, the maximum temperature of the cell array is reduced by 2.05 K, but the maximum temperature difference in the array showed a low reduction (less than 2 %). This shows that

Table 6: Parameters of interest for baseline and TPMS systems.

Item	Baseline System	TPMS System
Re,	75.0	23.1
$\overline{Nu}_{D2}$	6.76	21.05
$\overline{f}_{D2}$	0.82	17.52
$T_{max,b}$, K	304.02	301.97
$\Delta T_{max,b}$, K	2.056	2.024

the presence of TPMS-based structures influences the reduction of the maximum temperature of a battery cell, however, given the common configuration of the compared systems, it does not significantly improve the uniformity of temperatures in the battery cell, a factor potentially linked to the layout and number of tubes in the BTMS.

The behavior of $\overline{Nu}_x$ at each section taken by intervals of 2×10^{-3} m along the x axis in tube T2 is illustrated in Fig. 4. The expected behavior for a laminar flow is observed for the baseline system: high values near the entrance region of the tube due to the large temperature difference between wall and fluid (beginning of the development of the thermal boundary layer), but a reduction along the axis with an asymptotic approximation.

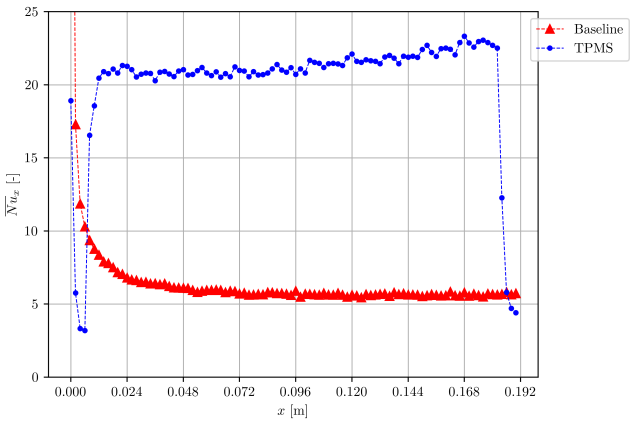

Figure 4: Local average Nusselt number evaluated in sections along the x axis for tube T2.

On the other hand, even though the TPMS-based system tube presents the same behavior in the inlet region there is an increase in the local average Nusselt number starting from $x = 8 \times 10^{-3}$ m. This point marks the beginning of the first TPMS-based unit structure. In addition, a slight growth of $\overline{Nu}_x$ along the x axis was observed, pointing out that greater values of $\overline{Nu}_x$ could be obtained if the channel could be extended in the x-direction, fact that was not observed in the baseline system. The previously described behavior can be explained due to the fact that the flow periodically recovers momentum along the x axis in the tubes of the TPMS system. The advection effects in the convective heat transfer process are intensified due to the maintenance of higher velocities along the tubes.

Figure 5 shows the phenomenon described above, in which the local average of the magnitude of velocity field is observed in sections taken by intervals of 2×10^{-3} m along the x axis in tube T2. Whereas in the tubes of the baseline system, the average velocity reaches an asymptotic value of 0.0115 m/s, the average velocity in the tube of the TPMS-based system varies periodically between 0.017 and 0.020 m/s in most part of the tube. Furthermore, there is an increase in $\overline{||\vec{V}||}_x$ from $x = 8 \times 10^{-3}$ m, coinciding with the increase in the Nusselt number (Fig. 4).

This relation between local average Nusselt number and $\overline{||\vec{V}||}_x$ along the x axis in the TPMS system is illustrated in more detail in Fig. 6. It is observed that, in the interval selected for the analysis, most of the intervals in which $\overline{Nu}_x$ grows, $\overline{||\vec{V}||}_x$ also increases with the exception of the point $x = 64 \times 10^{-3}$m .

Even though the periodic behavior of the mean velocity is directly related with the improvement in the convective heat transfer process, the spatial Fourier analysis, as illustrated in Fig. 7 and Fig. 8, does not show direct spatial correspondence with the wavenumber used in the construction of the TPMS-system.

While the $\overline{||\vec{V}||}_x$ DTFS magnitude shows significant periodic increases in mean velocity for wavenumbers with values of $\kappa = 125$ 1/m and $\kappa = 250$ 1/m (corresponding to wavelengths of, respectively, $x = 8 \times 10^{-3}$ m and $x = 4 \times 10^{-3}$ m), there is no direct correspondence for the local average Nusselt number. This behavior shows that the availability of a flow with periodic properties does not impact the heat transfer process with the same relevance.

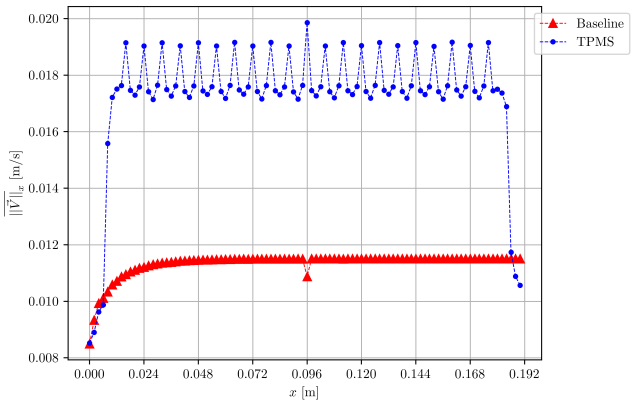

Figure 5: Local average of the magnitude of velocity field evaluated in sections along the x axis for tube T2.

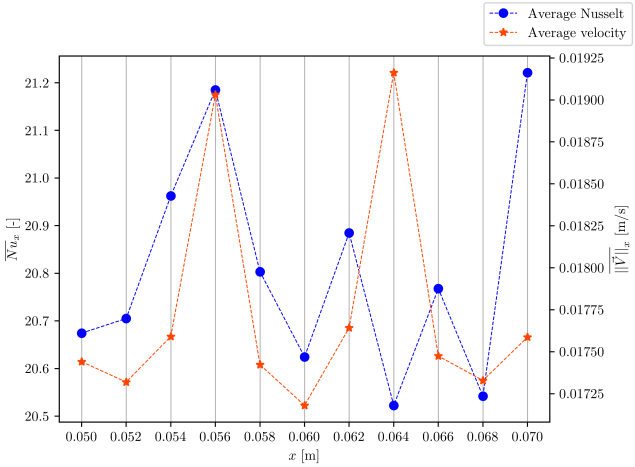

Figure 6: Local average Nusselt number and local average of the magnitude of velocity field over selected x axis range for TPMS-based geometry for tube T2.

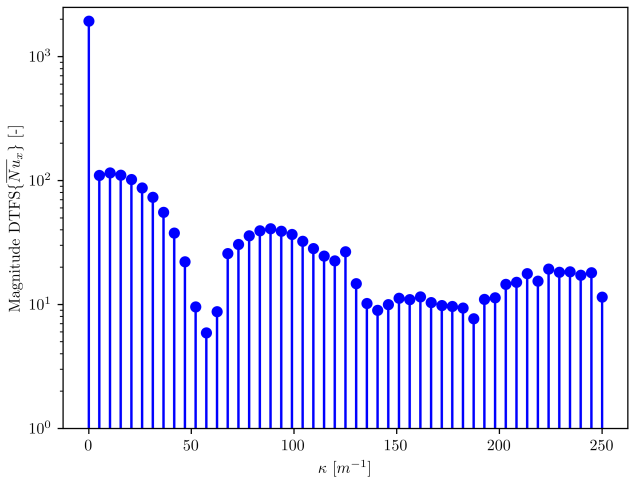

Figure 7: Spatial Fourier analysis of local average Nusselt number in T2 tube of TPMS system.

7. CONCLUSION

This work numerically investigated a liquid cooling BTMS based on Schwarz's Type-D TPMS. The analysis showed that the TPMS-based system enhances the battery cell cooling process compared to an empty tube BTMS (baseline system). The increase in surface area available for heat transfer between fluid and solid domains justifies this heat transfer enhancement. However, the global average friction factor associated with the TPMS-based BTMS is significantly higher than the baseline system.

Besides this, the TPMS system provides a better thermal operation to the battery cells, characterizing the use of a

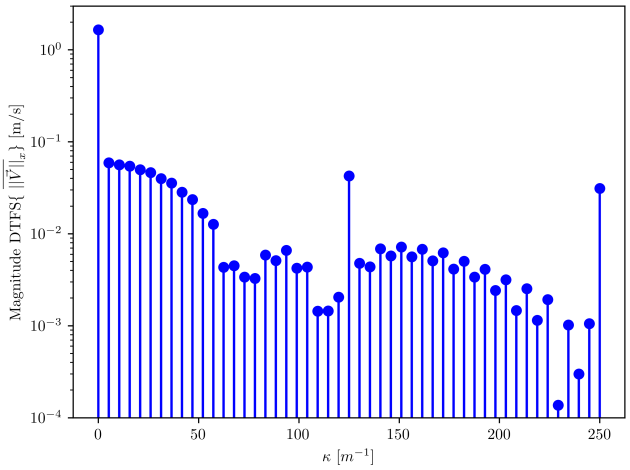

Figure 8: Spatial Fourier analysis of the local average of the magnitude of velocity field in T2 tube of the TPMS system.

TPMS system as a choice for better cooling capacity, but with a higher friction factor. Thus, numerical simulations for different operation points (mass flow and inlet temperature, for instance) can provide alternatives to reduce the high friction factor observed in the TPMS-based system.

For future works, other TPMS-based structures could be explored, such as Schwarz's types P and G, which can improve the cooling process of the BTMS. Lastly, modifications in the arrangement of TPMS structures inside the tubes and different flow orientations could be studied in order to explore the topological benefits of TPMS structures.

8. REFERENCES

Al-Ketan, O., Ali, M., Khalil, M., Rowshan, R., Khan, K.A. and Abu Al-Rub, R.K., 2021. "Forced Convection Computational Fluid Dynamics Analysis of Architected and Three-Dimensional Printable Heat Sinks Based on Triply Periodic Minimal Surfaces". *Journal of Thermal Science and Engineering Applications*, Vol. 13, No. 2, p. 021010. ISSN 1948-5085, 1948-5093. doi:10.1115/1.4047385.

Assis, M.M.S., 2021. *Forecast of the cost and support material in additive manufacturing through machine learning (in Portuguese)*. Master's thesis, Graduate Program in Production Engineer, Federal Univeristy of ABC, Santo André, Brasil.

Attarzadeh, R., Rovira, M. and Duwig, C., 2021. "Design analysis of the "Schwartz D" based heat exchanger: A numerical study". *International Journal of Heat and Mass Transfer*, Vol. 177, p. 121415. ISSN 00179310. doi:10.1016/j.ijheatmasstransfer.2021.121415.

Celik, I., Ghia, U., Roache, P., Freitas, C., Coloman, H. and Raad, P., 2008. "Procedure of estimation and reporting of uncertainty due to discretization in cfd applications". *J. Fluids Eng.*, Vol. 130, p. 078001. doi:10.1115/1.2960953.

Deng, Y., Feng, C., E, J., Zhu, H., Chen, J., Wen, M. and Yin, H., 2018. "Effects of different coolants and cooling strategies on the cooling performance of the power lithium ion battery system: A review". *Applied Thermal Engineering*, Vol. 142, pp. 10–29. ISSN 1359-4311. doi:10.1016/j.applthermaleng.2018.06.043.

Fan, Z., Gao, R. and Liu, S., 2022. "A novel battery thermal management system based on P type triply periodic minimal surface". *International Journal of Heat and Mass Transfer*, Vol. 194, p. 123090. ISSN 0017-9310. doi:10.1016/j.ijheatmasstransfer.2022.123090.

Han, T., Khalighi, B., Yen, E.C. and Kaushik, S., 2019. "Li-Ion Battery Pack Thermal Management: Liquid Versus Air Cooling". *Journal of Thermal Science and Engineering Applications*, Vol. 11, No. 2, p. 021009. ISSN 1948-5085, 1948-5093. doi:10.1115/1.4041595.

He, C., Li, M., Wang, F. and Zheng, J., 2022. "Simulation study of a cylindrical battery module". *Journal of Energy Storage*, Vol. 48, p. 104000. ISSN 2352152X. doi:10.1016/j.est.2022.104000.

Ianniciello, L., Biwolé, P.H. and Achard, P., 2018. "Electric vehicles batteries thermal management systems employing phase change materials". *Journal of Power Sources*, Vol. 378, pp. 383–403. ISSN 0378-7753. doi:10.1016/j.jpowsour.2017.12.071.

Incropera, F.P., ed., 2007. *Fundamentals of heat and mass transfer*. John Wiley, Hoboken, NJ, 6th edition. ISBN 9780471457282. OCLC: ocm62532755.

International Energy Agency, 2020. *Global EV Outlook 2020: Entering the decade of electric drive?* Global EV Outlook. OECD. ISBN 9789264616226. doi:10.1787/d394399e-en.

International Energy Agency, 2022. *Global EV Outlook 2022: Securing supplies for an electric future*. Global EV Outlook. OECD. ISBN 9789264898875. doi:10.1787/c83f815c-en.

Kim, J., Oh, J. and Lee, H., 2019. "Review on battery thermal management system for electric vehicles". *Applied Thermal Engineering*, Vol. 149, pp. 192–212. ISSN 1359-4311. doi:10.1016/j.applthermaleng.2018.12.020.

Peng, H., Gao, F. and Hu, W., 2019. "Design, Modeling and Characterization on Triply Periodic Minimal Surface Heat Exchangers with Additive Manufacturing". In *2019 International Solid Freeform Fabrication Symposium*. University of Texas at Austin. doi:10.26153/tsw/17483. URL `https://repositories.lib.utexas.edu/handle/2152/90564`.

Rajagopalan, S. and Robb, R., 2006. "Schwarz meets Schwann: Design and fabrication of biomorphic and durataxic tissue engineering scaffolds". *Medical Image Analysis*, Vol. 10, No. 5, pp. 693–712. ISSN 13618415. doi:10.1016/j.media.2006.06.001.

Rao, Z., Qian, Z., Kuang, Y. and Li, Y., 2017. "Thermal performance of liquid cooling based thermal management system for cylindrical lithium-ion battery module with variable contact surface". *Applied Thermal Engineering*, Vol. 123, pp. 1514–1522. ISSN 1359-4311. doi:10.1016/j.applthermaleng.2017.06.059.

Tang, W., Zhou, H., Zeng, Y., Yan, M., Jiang, C., Yang, P., Li, Q., Li, Z., Fu, J., Huang, Y. and Zhao, Y., 2023. "Analysis on the convective heat transfer process and performance evaluation of Triply Periodic Minimal Surface (TPMS) based on Diamond, Gyroid and Iwp". *International Journal of Heat and Mass Transfer*, Vol. 201, p. 123642. ISSN 00179310. doi:10.1016/j.ijheatmasstransfer.2022.123642.

Tete, P.R., Gupta, M.M. and Joshi, S.S., 2022. "Numerical investigation on thermal characteristics of a liquid-cooled lithium-ion battery pack with cylindrical cell casings and a square duct". *Journal of Energy Storage*, Vol. 48, p. 104041. ISSN 2352-152X. doi:10.1016/j.est.2022.104041.

Versteeg, H.K. and Malalasekera, W., 2007. *An introduction to computational fluid dynamics: the finite volume method*. Pearson Education Ltd, Harlow, England ; New York, 2nd edition. ISBN 9780131274983. OCLC: ocm76821177.

Wang, H., Wang, Y., Hu, F., Shi, W., Hu, X., Li, H., Chen, S., Lin, H. and Jiang, C., 2021. "Heat generation measurement and thermal management with phase change material based on heat flux for high specific energy power battery". *Applied Thermal Engineering*, Vol. 194, p. 117053. ISSN 13594311. doi:10.1016/j.applthermaleng.2021.117053.

Wang, H., Tao, T., Xu, J., Mei, X., Liu, X. and Gou, P., 2020. "Cooling capacity of a novel modular liquid-cooled battery thermal management system for cylindrical lithium ion batteries". *Applied Thermal Engineering*, Vol. 178, p. 115591. ISSN 1359-4311. doi:10.1016/j.applthermaleng.2020.115591.

9. RESPONSIBILITY NOTICE

The author(s) is (are) solely responsible for the printed material included in this paper.